



# Thermal Equation of State of Natural F-Rich Topaz up to 29 GPa and 750 K

Yungui Liu<sup>1,2</sup>, Xiang Li<sup>1</sup>, Haipeng Song<sup>1</sup>, Jingui Xu<sup>3</sup>, Dongzhou Zhang<sup>3</sup>, Junfeng Zhang<sup>1</sup>,  
Xiang Wu<sup>1\*</sup>

1. State Key Laboratory of Geological Processes and Mineral Resources, China University of Geosciences, Wuhan 430074, China

2. College of Gems and Materials, Hebei GEO University, Shijiazhuang 050031, China

3. Hawai'i Institute of Geophysics and Planetology, School of Ocean and Earth Science and Technology, University of Hawaii at Manoa, Honolulu HI 96822, USA

 Yungui Liu: <https://orcid.org/0000-0003-4493-5476>;  Xiang Wu: <https://orcid.org/0000-0002-3249-168X>

**ABSTRACT:** Subducting oceanic sediments and crusts, originating from the Earth's surface and descending into its deep interior, are important carriers of volatiles. The volatiles have significant effects on materials cycling and the dynamic evolution of the subduction zones. A simplified  $\text{Al}_2\text{O}_3\text{-SiO}_2\text{-H}_2\text{O}$  (ASH) ternary system models the relationship of minerals in the hydrated and alumina-silica rich sedimentary layer. Topaz  $\text{Al}_2\text{SiO}_4(\text{F,OH})_2$  is an important mineral in the ASH system and comprises two volatiles:  $\text{H}_2\text{O}$  and fluorine (F). In this study, the thermoelasticity of a natural F-rich topaz was investigated using synchrotron-based single-crystal X-ray diffraction combined with diamond anvil cells up to 29.1 GPa and 750 K. The pressure-volume-temperature data were fitted to a third-order Birch-Murnaghan Equation of state with  $V_0 = 343.15(7) \text{ \AA}^3$ ,  $K_0 = 166(1) \text{ GPa}$ ,  $K_0' = 3.0(1)$ ,  $(\partial K_0/\partial T)_p = -0.015(9) \text{ GPa/K}$  and  $\alpha_0 = 3.9(5) \times 10^{-5} \text{ K}^{-1}$ . The isothermal bulk modulus increases with the F content in topaz, and the various F contents present significant effects on its anisotropic compressibility. Our results further reveal that the isothermal bulk modulus  $K_0$  of the minerals in ASH system increases with density. F and H contents in hydrous minerals might greatly affect their properties (e.g., compressibility and stability), providing more comprehensive constraints on the subduction zones.

**KEY WORDS:** topaz, hydrous mineral, water, fluorine, subduction zones.

## 0 INTRODUCTION

Volatiles, such as  $\text{H}_2\text{O}$  and halogens, play key roles in the dynamic evolution of the Earth's interior and the geochemical cycling of materials between the crust and mantle (Wang et al., 2020; Bucher and Stober, 2019; Galvez et al., 2016; Turner et al., 2012; Zhu et al., 2011). Hydrogen is probably the most abundant and consequently the most important volatile component in the deep earth, it can significantly affect the elasticity, rheology and transport properties of mantle rocks in the conditions of the Earth's interior (Huang et al., 2019; Ohtani et al., 2018; Nakagawa, 2017). Subduction zones are supposed to be the primary locations where surface water is delivered into deep earth, high pressure and high temperature (HPHT) experiments reveal that water reserved in the slabs can be transported into the depth of the transition zone and lower mantle even in relatively hot subduction slabs (Faccenda, 2014; Nishi et al., 2014). Recently, limited attention has been paid to the deep subduction of fluorine (F), which is probably the most abundant

halogen in the Earth's mantle (e.g., Li X et al., 2020; Grützner et al., 2018; Yoshino and Jaseem, 2018). Halogens (F, Cl, Br, I) are enriched in marine sediments, the altered oceanic crust and the serpentinized mantle lithosphere (Barnes et al., 2018). Compared to other heavy halogen elements (Cl, Br and I), which are hydrophilic, F behaves as a lithophile element and is never significantly extracted by degassing processes (Barnes et al., 2018; Balcone-Boissard et al., 2010; Bureau et al., 2000). Thus, F is likely to be retained in subducting slabs compared to other heavy halogens during devolatilization processes. It is estimated that 95% of the subducted F has been believed to be transported down to mantle depths (Straub and Layne, 2003). The hydroxyl group is often substituted by F in hydrous minerals because of the similarity of F<sup>-</sup> and OH<sup>-</sup> both in ionic charge and radius (e.g., Ross and Crichton, 2001); therefore, certain amounts of F might be incorporated into subducting hydrous minerals and transported into the Earth's deep interior.

Topaz is an F/OH-bearing aluminosilicate mineral with the ideal formula  $\text{Al}_2\text{SiO}_4(\text{F,OH})_2$ . F is dominant in natural topaz and generally the substitution of F by OH only occurs to a limited extent ( $\text{OH}/(\text{OH} + \text{F}) < 0.5$ ) (Gatta et al., 2014). The highest OH content of topaz ( $\text{OH}/(\text{OH} + \text{F}) = 0.55$ ) was found in the ultrahigh-pressure belts of the Sulu terrane, China (Zhang et al., 2002). The content of OH in natural topaz is controlled by the crystallization temperature and pressure condi-

\*Corresponding author: [wuxiang@cug.edu.cn](mailto:wuxiang@cug.edu.cn)

© China University of Geosciences (Wuhan) and Springer-Verlag GmbH Germany, Part of Springer Nature 2023

Manuscript received December 21, 2020.

Manuscript accepted January 20, 2021.

tions (Wunder et al., 1999). Instead, the OH endmember topaz-OH  $\text{Al}_2\text{SiO}_4(\text{OH})_2$  was first synthesized at pressures between 5.5 and 10 GPa and temperatures up to 1 000 °C by Wunder et al. (1993). Many studies have focused on the crystal chemistry of the solid solution series  $\text{Al}_2\text{SiO}_4\text{F}_2$ - $\text{Al}_2\text{SiO}_4(\text{OH})_2$  to determine the location of protons (H) (e.g., Watenphul et al., 2010; Churakov and Wunder, 2004). The space group of natural topaz belongs to  $Pbnm$  ( $Z = 4$ ) with one independent H-site, while topaz-OH displays two nonequivalent H-sites. Although topaz-OH was initially regarded as belonging to the lower symmetry  $Pbn2_1$  (Northrup et al., 1994), subsequent studies suggested that its space group should also be  $Pbnm$  (Komatsu et al., 2008; Chen et al., 2005).

At the top of the subducting slab, pelagic sediments and oceanic crusts have greater alumina and silica than mafic mantle rocks. It has been indicated that the hydrous aluminosilicate phases (simplified in the  $\text{Al}_2\text{O}_3$ - $\text{SiO}_2$ - $\text{H}_2\text{O}$  (ASH) system) have significantly greater thermal stability than the magnesio-silicate hydrous phases based on the HPHT experiments and are likely to be important reservoirs of water in subduction zones (Duan et al., 2018; Pamato et al., 2015). Previous studies have shown that topaz-OH could occur as one of the breakdown products of phengite or lawsonite and can be stable up to 12 GPa and 1 100 °C (Ono, 1998); accordingly, it might play an important role in water transportation at the depth of the upper mantle. On the other hand, the accommodation of F in phengite and lawsonite suggests that F could be transported to a depth of 300 km in the cold subduction zones and has contributed to the deep cycling of F (Pagé et al., 2018, 2016). The eventual decomposition of phengite and lawsonite may lead to a redistribution of F in topaz, and thus topaz might be an important potential carrier of hydroxyl groups and F in subduction zones.

Here, we conducted single crystal X-ray diffraction (XRD) experiments of natural topaz  $\text{Al}_2\text{SiO}_4\text{F}_{1.64}(\text{OH})_{0.36}$  up to 23.7 GPa at room temperature to explore the influence of F and OH on its compressibility. We simultaneously measured its thermal equation of state (EoS) up to 29.1 GPa and 750 K using an external heating diamond anvil cell (DAC). We focused on the compositional and temperature range over which the high-pressure behavior of F/OH-bearing topaz can be modeled. The results will improve our understanding of the effects of F and hydroxyl groups in hydrous phases and provide feedback for volatiles deep cycling and the constraints on the fine seismic velocity profiles in subduction zones.

## 1 METHODS

A gem-quality, pale blue and transparent, natural single crystal of topaz was used for this study. Sample characterizations were performed using electron microprobe analysis, XRD and Raman spectroscopy. Analysis of the chemical compositions was conducted with a JEOL JXA-8100 electron probe microanalyzer at China University of Geosciences (Wuhan), operating with an acceleration voltage of 15 kV and beam current of 20 nA. The chemical formula was determined to be  $\text{Al}_2\text{SiO}_4\text{F}_{1.64}(\text{OH})_{0.36}$ . The crystal structure was determined to be orthorhombic phase ( $Pbnm$  and  $Z = 4$ ) with lattice constants of  $a = 4.648\ 3(1)$  Å,  $b = 8.795\ 3(2)$  Å,  $c = 8.388\ 3(2)$  Å, and  $V = 342.94(1)$  Å<sup>3</sup> by a XtaLAB PRO MM007HF single-crystal X-

ray diffractometer equipped with Cu  $K\alpha$  radiation at Huazhong University of Science and Technology, Wuhan. The crystal structure (Fig. 1) was drawn by the VESTA software (Momma and Izumi, 2011). The Raman spectra were collected by a HORIBA LabRAM HR Evolution spectrometer equipped with a 532 nm laser at China University of Geosciences (Wuhan). The OH concentrations in topaz as a function of the position of Raman band attributed to the stretching mode of the hydroxyl group has been reported by Pinheiro et al. (2002). We fitted the Raman peak using Lorentz function and the fitting standard error is  $0.02\ \text{cm}^{-1}$ . Accordingly, the electron microprobe analysis result is in good agreement with the calculated OH content based on the Raman spectrum (Fig. S1).

A short symmetry-type DAC equipped with Boehler-type diamond anvils (400- $\mu\text{m}$  flat culets with 60° opening) was employed to achieve high pressure for room temperature experiments (Boehler, 2006). A 260- $\mu\text{m}$ -diameter hole was drilled in a 35  $\mu\text{m}$ -thick pre-indented rhenium gasket as the sample chamber. A single-crystal sample of grain size  $\sim 20 \times 35 \times 15\ \mu\text{m}^3$  was loaded into the sample chamber. Platinum and neon were employed as the pressure scale and pressure transmitting medium, respectively (Rivers et al., 2008; Fei et al., 2007). *In situ* high-pressure single crystal XRD experiments were carried out at beamline 13-BMC of the Advanced Photon Source (APS), Argonne National Laboratory (ANL) (Zhang et al., 2017). A monochromatic X-ray beam with a wavelength of 0.434 09 Å was focused on a  $15 \times 15\ \mu\text{m}^2$  spot. The sample-to-detector distance and beam center positions were calibrated using a  $\text{LaB}_6$  standard. The XRD patterns were recorded with a Pilatus3 1M detector. Stepped exposures were collected in a rotation range from  $-30^\circ$  to  $30^\circ$  with a  $1^\circ$  step, and the exposure time was 3 seconds per frame. Experimental data were analyzed using Bruker APEX3 software.

*In situ* HPHT single crystal XRD experiments were conducted up to 29.1 GPa at four temperatures (300, 450, 600 and 750 K) at beamline 13-BMC of the APS. A BX90-type DAC equipped with 400- $\mu\text{m}$  flat culet diamond anvils was used for HPHT experiments (Kantor et al., 2012). A double-polished single-crystal sample with a size of  $\sim 20 \times 30 \times 15\ \mu\text{m}^3$  was

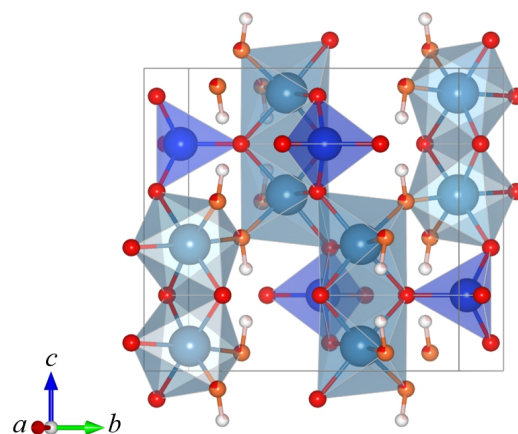


**Figure 1.** The crystal structure of topaz in this study under ambient conditions (space group  $Pbnm$ ,  $Z = 4$ ). The blue, tile blue, red, orange and pink balls represent Si, Al, O, F and H atoms, respectively. The color divided balls represent the site occupancies.

loaded into the chamber, which was prepared in the same manner as the high-pressure experiments. Platinum and neon were used as the pressure marker and pressure transmitting medium, respectively (Rivers et al., 2008; Fei et al., 2007). One platinum wire that was 200  $\mu\text{m}$  in diameter and approximately 45 cm in length was coiled around the alumina ceramic, which was used as a ring heater, and its resistance was approximately  $2\ \Omega$ . A K-type thermocouple attached to one of the diamond anvils and close to the sample chamber was used to determine the temperatures, and the thermal gradients between thermocouple and sample were less than 25 K in our experiments (Fan et al., 2010). The GE PACE5000 membrane pressure controller at the beamline 13-BMC was employed to remotely increase the pressure. For each pressure-temperature ( $P$ - $T$ ) point, the sample chamber was stabilized for at least 20 minutes to minimize the thermal gradient and pressure instability. Due to the limitation of the heater, the opening angle of the high-temperature DAC is limited, and the diffraction peaks are not enough to reconstruct a 3-D lattice in reciprocal space. The step scan images were merged into a single image file, and the merged image was integrated using Dioptas software (Prescher and Prakapenka, 2015). The  $d$ -spacing of each available diffraction peak was then fitted, and the UnitCell program was used to calculate the lattice parameters (Holland and Redfern, 1997). The  $P$ - $V$  data,  $P$ - $V$ - $T$  data and  $P$ - $x$  (i.e.,  $a/b/c$  axes) data were fitted by the Eos-Fit7-GUI program (Gonzalez-Platas et al., 2016).

## 2 RESULTS AND DISCUSSION

Natural F-rich topaz was compressed up to 23.7 GPa at room temperature and no phase transition was observed over this pressure range. The lattice parameters are summarized in Table S1 and the examples of recorded XRD patterns at differ-

ent pressures are presented in Fig. S2. The unit cell volumes monotonously decrease with increasing pressure, compared with those of previous studies shown in Fig. 2 (Ulian and Valdrè, 2017; Mookherjee et al., 2016; Gatta et al., 2014, 2006; Komatsu et al., 2008, 2003). The volume dependence of pressure is adequately described by a third-order Birch-Murnaghan equation of state (BM EoS) (Gonzalez-Platas et al., 2016; Angel et al., 2014). The derived EoS parameters are as follows:  $V_0 = 343.15(14)\ \text{\AA}^3$ ,  $K_0 = 166(3)\ \text{GPa}$ , and  $K_0' = 3.0(2)$ , which are consistent with the previous studies on natural topaz with little difference in the amounts of F from the present study (Gatta et al., 2014, 2006) and the results from F-bearing topaz based on the first-principle simulations (Ulian and Valdrè, 2017). However, the  $K_0$  in this study is significantly larger than the values of synthesized OH(D)-endmember topaz from Grevel et al. (2000b) with  $K_0 = 143(2)\ \text{GPa}$  and Chen and Larger (2005) with  $K_0 = 145(4)\ \text{GPa}$ .

Topaz is a representative aluminosilicate mineral containing F and OH. A recent study has demonstrated that F and OH contents have important effects on the elasticity and sound velocity of topaz under high temperature conditions (Tennakoon et al., 2018). In our present study, we explored the effects on isothermal bulk moduli and their pressure derivatives of topaz caused by various F/OH contents at high pressures. The normalized stress ( $F_E = P/[3f_E(2f_E + 1)^{5/2}]$ ) as a function of the Eulerian finite strain ( $f_E = [(V_0/V)^{2/3} - 1]/2$ ) of topaz from our present experiments and previous studies (Gatta et al., 2014, 2006; Komatsu et al., 2008, 2003) are plotted in Fig. S3. The linear  $f_E$ - $F_E$  relationships suggest that the third-order BM EoS is adequate, and the negative and positive slopes indicate that  $K' < 4$  and  $K' > 4$ , respectively (Angel, 2000). Isothermal bulk moduli and their pressure derivatives of topaz in this and previous stud-

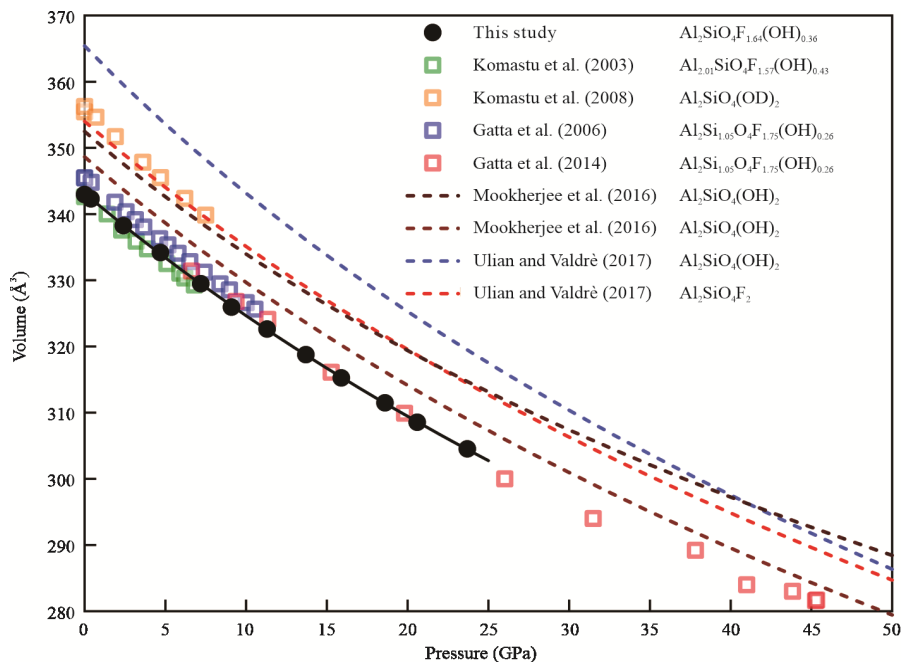


**Figure 2.** Unit cell volumes of topaz as a function of pressure. The solid black circles, open orange and green squares and red and blue squares represent the experimental data from this study, Komatsu et al. (2008, 2003) and Gatta et al. (2014, 2006) at ambient temperature, respectively. The solid black line represents the fitting result from our data using the third-order BM EoS. The dashed dark wine-red (monoclinic topaz-OH), wine (orthorhombic topaz-OH), blue and red lines represent the theoretical calculation results from Mookherjee et al. (2016), Ulian and Valdrè (2017) at 0 K. The error bars are smaller than the symbol size for our data.

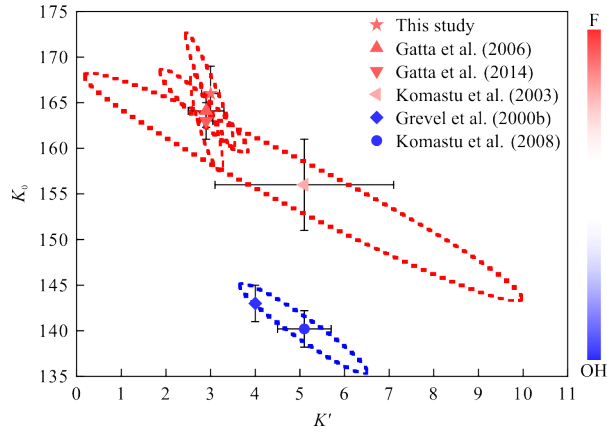


**Figure 3.** Isothermal bulk moduli and their pressure derivatives of topaz from this study and literature values plotted as confidence ellipsoids at the 95.4% level. The chemical formulas are as follows:  $\text{Al}_2\text{SiO}_4\text{F}_{1.64}(\text{OH})_{0.36}$  (this study),  $\text{Al}_{2.01}\text{SiO}_4\text{F}_{1.57}(\text{OH})_{0.43}$  (Komastu et al., 2003),  $\text{Al}_2\text{Si}_{1.05}\text{O}_4\text{F}_{1.75}(\text{OH})_{0.26}$  (Gatta et al., 2014, 2006),  $\text{Al}_2\text{SiO}_4(\text{OD})_2$  (Komastu et al., 2008) and  $\text{Al}_2\text{SiO}_4(\text{OH})_2$  (Grevel et al., 2000b).

ies are plotted in Fig. 3. The contrastive results reveal that increasing the substitution of F for OH in topaz leads to its structure being less compressible. This finding is consistent with the first-principle simulation study on the compressional behavior of different F contents of topaz, in which the zero pressure athermal bulk modulus  $K_0$  increases with the F content (Ulian and Valdrè, 2017).

The HPHT single crystal XRD data of natural F-rich topaz were collected up to 29.1 GPa and 750 K. The  $P$ - $V$ - $T$  data are plotted in Fig. 4, and lattice parameters are summarized in Table S1. Both the unit cell volumes under high-pressure at room temperature and HPHT conditions were used to fit the third-order BM thermal EoS as follows (Angel et al., 2014)

$$P(V, T) = \frac{3}{2} K_{T_0} \left[ \left( \frac{V_{T_0}}{V} \right)^{\frac{7}{3}} - \left( \frac{V_{T_0}}{V} \right)^{\frac{5}{3}} \right] \times \left\{ 1 + \frac{3}{4} (K'_{T_0} - 4) \left[ \left( \frac{V_{T_0}}{V} \right)^{\frac{2}{3}} - 1 \right] \right\} \quad (1)$$

$$V_{T_0} = V_0 \exp \int_{300}^T \alpha_T dT \quad (2)$$

$$K_{T_0} = K_0 + \left( \partial K_0 / \partial T \right)_P \times (T - 300) \quad (3)$$

$$\alpha_T = \alpha_0 + \alpha_1 T + \alpha_2 T^2 \quad (4)$$

where  $K_{T_0}$ ,  $K'_{T_0}$  and  $V_{T_0}$  are isothermal bulk modulus, its first pressure derivative, and unit-cell volume at temperature  $T$  and ambient pressure, respectively.  $V_{T_0}$  (thermal dependence of the zero-pressure volume) and bulk modulus  $K_{T_0}$  on different isotherms are given in the expressions (2) and (3), respectively.  $V_0$  is the unit-cell volume at ambient conditions.  $K_0$  is the reference bulk modulus at ambient conditions.  $\alpha_T$  is thermal expansion coefficient at temperature  $T$  and ambient pressure, it is proposed to be a function of temperature by Fei and defined in the expressions (4) (Fei, 1995). The limited number of high-pressure high-

temperature data points and the relatively limited temperature range (300–750 K) of our experiments might prevent a reasonable result of  $\alpha_1$  and  $\alpha_2$  (Nishihara et al., 2003), so we treated thermal expansion coefficient as a constant in this study and yielded the average thermal expansion coefficient  $\alpha_0$ . The thermoelastic parameters (summarized in Table S2) derived from the fits are as follows:  $V_0 = 343.15(7) \text{ \AA}^3$ ,  $K_0 = 166(1) \text{ GPa}$ ,  $K'_0 = 3.0(1)$ ,  $(\partial K_0 / \partial T)_P = -0.015(9) \text{ GPa/K}$ , and  $\alpha_0 = 3.9(5) \times 10^{-5} \text{ K}^{-1}$ . The fitting results of  $V_0$ ,  $K_0$ , and  $K'$  between the thermal EoS and the  $P$ - $V$  data at room temperature are mutually equivalent. The negative  $\partial K_0 / \partial T$  value indicates that the bulk modulus of topaz decreases with the increase of temperature. Komastu et al. (2003) measured the thermal expansion of F-rich topaz ( $\text{Al}_{2.01}\text{SiO}_4\text{F}_{1.57}(\text{OH})_{0.43}$ ) from 298 to 1 173 K at room pressure by powder XRD. The derived volume thermal expansivity  $\alpha_0$  is  $2.0(1) \times 10^{-5} \text{ K}^{-1}$ , which is smaller than our result for  $\text{Al}_2\text{SiO}_4\text{F}_{1.64}(\text{OH})_{0.36}$  considering the standard deviation. The slight difference in compositions (amounts of F or OH) should be considered, but that should not be the main reason. For the reason that thermal expansion coefficient  $\alpha_T$  is correlated with the temperature range, we fitted the  $V$ - $T$  data from Komastu et al. (2003) at the temperature range of 298–723 K by Fei Equation, which corresponds to the temperature range of our experiments. Here, we treated  $\alpha_T$  as a linear function of temperature because the third item  $\alpha_2 T^2$  is small at high temperature and can be ignored. The results yielded are as follows:  $\alpha_0 = 3.8(16) \times 10^{-5} \text{ K}^{-1}$ ,  $\alpha_1 = -3.2(32) \times 10^{-8} \text{ K}^{-2}$ ,  $\alpha_0$  is identified with our results, but  $\alpha_1$  is unreasonable. If we treated thermal expansion coefficient as a constant and obtained the average thermal expansion coefficient  $\alpha_0 = 2.3(2) \times 10^{-5} \text{ K}^{-1}$ . There are only four  $V$ - $T$  data points between 298 and 750 K at ambient pressure for both this study and results from Komastu et al. (2003). Both of the two values of  $\alpha_0$  are higher than  $2.0(1) \times 10^{-5} \text{ K}^{-1}$ . Previous studies on thermal expansion coefficients of hydrous minerals, carbonate minerals and silicate minerals also indicate inconsistency. For example, the thermal expansion coefficient  $\alpha_0$  ( $5$  to  $6) \times 10^{-5} \text{ K}^{-1}$ ) from HPHT experiments is much larger than high-temperature experimental results at ambient pressure ( $3.68(6) \times 10^{-5} \text{ K}^{-1}$ ) of clinohumite (Qin et al., 2017; Ye et al., 2013); the average thermal expansion coefficient  $\alpha_0$  of calcite varies from  $1.6 \times 10^{-5}$  to  $2.9 \times 10^{-5} \text{ K}^{-1}$ , despite using the same temperature range (Wang et al., 2019); the thermal expansion coefficient of pyrope at 300 K varies from  $1.6 \times 10^{-5}$  to  $3.0 \times 10^{-5} \text{ K}^{-1}$  based on the different researches (Hartwig and Galkin, 2021); the  $\alpha_T$  of forsterite taken from different literatures also shows considerable discrepancies (Kroll et al., 2012). On the other hand, the thermal expansion coefficient  $\alpha_0$  and  $\partial K_0 / \partial T$  in BM thermal EoS are coupled with each other. Thus, we propose that more experiments under HPHT conditions with smaller temperature interval and wider temperature range should be conducted to obtain accurate thermal expansion coefficient, which will provide more reliable thermodynamic data to constrain the dynamical model of Earth.

Normalized axial compression data of F-rich topaz in this study and deuterated topaz (topaz-OD) (Komastu et al., 2008) at high pressure and room temperature are plotted in Fig. 5a. A linearized third-order BM EoS fitting where each axial dimension is cubed and treated as volume in the BM formulation

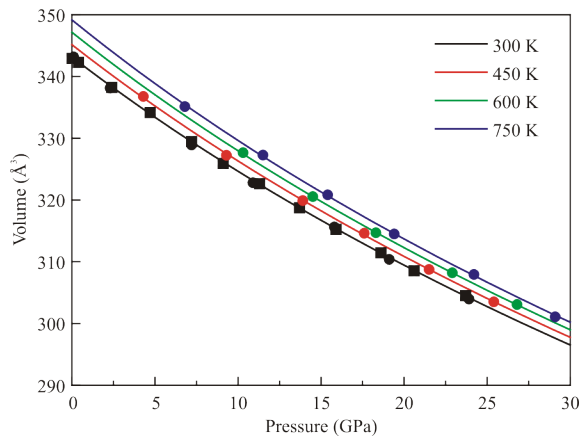


**Figure 4.**  $P$ - $V$ - $T$  data obtained for topaz in this study. The solid lines represent the isothermal compression curves from the high temperature third-order BM EoS at 300, 450, 600 and 750 K, respectively. The gray circles represent the high-pressure experimental data at room temperature in this study. The error bars are smaller than the symbol size.

was used to compare the axial compressibility of  $a$ ,  $b$ , and  $c$  (Gonzalez-Platas et al., 2016; Angel et al., 2014). The zero-pressure axial compressibility of linear dimension  $l$ , defined as  $\beta_{l0} = -(l^{-1})(\delta l/\delta P)_{P=0}$ , is related to the linear modulus by  $M_{l0} = (\beta_{l0})^{-1}$ , and the linear moduli and their pressure derivatives defined in this way have numerical values three times those of the corresponding volume bulk modulus, i. e.,  $M(i) = 3K_0(i)$  and  $M'(i) = 3K'_0(i)$  (Angel et al., 2014). The fitted linear moduli and their pressure derivatives of  $a$ ,  $b$ , and  $c$  are as follows:  $M_a = 463(8)$  GPa,  $M'_a = 7.4(7)$ ,  $M_b = 660(17)$  GPa,  $M'_b = 9.0(14)$ ,  $M_c = 431(9)$  GPa,  $M'_c = 9.7(8)$  for the F-rich topaz in this study, corresponding to axial compressibility values of  $\beta_a = 2.16(4) \times 10^{-3}$  GPa $^{-1}$ ,  $\beta_b = 1.52(4) \times 10^{-3}$  GPa $^{-1}$ , and  $\beta_c = 2.32(5) \times 10^{-3}$  GPa $^{-1}$  ( $\beta_a : \beta_b : \beta_c = 1.42 : 1.00 : 1.53$ ). These values are consistent well with the results of  $\beta_a : \beta_b : \beta_c = 1.47 : 1.00 : 1.63$  in consideration of the small differences in component from Gatta et al. (2006). For comparison, we refitted the data of topaz-OD from Komatsu et al. (2008) using the third-order BM EoS and presented the results in Table S3. The obtained linear moduli for the  $a$ ,  $b$ , and  $c$  axes are as follows:  $M_a = 469(13)$  GPa,  $M'_a = 19(4)$ ,  $M_b = 548(24)$  GPa,  $M'_b = 10(6)$ ,  $M_c = 310(6)$  GPa and  $M'_c = 15.6(19)$ , which correspond to axial compressibility values of  $\beta_a = 2.13(6) \times 10^{-3}$  GPa $^{-1}$ ,  $\beta_b = 1.83(8) \times 10^{-3}$  GPa $^{-1}$ , and  $\beta_c = 3.23(6) \times 10^{-3}$  GPa $^{-1}$  ( $\beta_a : \beta_b : \beta_c = 1.16 : 1.00 : 1.77$ ), indicating consistent results on the anisotropic axial compressibility with least-squares fits ( $\beta_a : \beta_b : \beta_c = 1.09 : 1.00 : 1.60$ ) by Komatsu et al. (2008). It is reported that H/D isotope effects can affect the anisotropic of axial compressional behaviors. However, the effects of deuteration depend on the  $(O \cdots O)_{\text{H/D}}$  distance, which will be significant when the distance is in the range of 2.43–2.65 Å (Sano-Furukawa et al., 2009). Accordingly, there should be no significant isotope effects on the anisotropy of axial compressibility of topaz-OD, because of its larger  $(O \cdots O)_b$  distance ( $>2.99$  Å) (Komatsu et al., 2008). The compressibilities of the  $a$ ,  $b$ , and  $c$  axes are distinguishable from each other with a consideration of the trade-off between the linear moduli and their pressure derivatives (Fig. 5b). Both phases reveal a significant anisotropy in axial compressibilities with  $\beta_c > \beta_a > \beta_b$ , but the axial com-

pressional behaviors are influenced by the contents of F (or hydroxyl). It is revealed that increasing the F content leads to the  $b$ -axis and  $c$ -axis becoming relatively harder to compress while increasing the compressibility of the  $a$ -axis. The influence of the F content on the axial compressional behavior was also reported on chondrodite (Friedrich et al., 2002). Crystal chemistry studies revealed that the substitution of hydroxyl groups by F induces reductions in the Al-(O,F) internal bond lengths and Al(O,F) $_6$  polyhedral volumes and changes in the distortion index of the Al(O,F) $_6$  polyhedra, which will lead to variations in the compression responses of polyhedral contraction and tilting direction (Ulian and Valdrè, 2017). Furthermore, the frames of one independent H-site in F-rich topaz and two nonequivalent H-sites in topaz-OH display different hydrogen bonding geometries, and correspondingly, various pressure responses in different directions have been observed (Ulian and Valdrè, 2017; Komatsu et al., 2008). Thus, the above atomic-scale compression mechanisms are employed to explain the effects of the F content on the axial compressibilities. The anisotropy of axial compressibility and thermal expansion of F-rich topaz are also closely related to its crystal structure. The O-H covalent bond in F-rich topaz is almost perpendicular to  $b$  axis and forms a small angle with  $c$  axis, leading to a repulsion effect between the neighboring H atoms along the direction of O-H bond. Therefore,  $c$  axis will be the softest and most expansion direction, while  $b$  axis will be the hardest and least expansion direction, which are consistent well with the experimental results on axial compressibility in this study and axial thermal expansivity (Komatsu et al., 2003).

### 3 IMPLICATIONS

There is a wealth of knowledge regarding water transport by descending slabs and its implications for geodynamic processes. Nevertheless, other volatile elements, such as carbon, sulfur, nitrogen and halogens, draw increasingly more attention because they may also have significant effects on subduction processes, especially under the Earth's upper mantle conditions (Li X Y et al., 2020; Hughes and Pawley, 2019). The hydrous phases with hydroxyl groups in their formula (e.g., serpentine, amphibole, mica, lawsonite and humite-type minerals) are regarded as important carriers of volatiles (Pagé et al., 2018, 2016). It is anticipated that F (25  $\mu\text{g/g}$ ) is more than one tenth of the  $\text{H}_2\text{O}$  (50–200  $\mu\text{g/g}$ ) in the primitive mantle (McDonough and Sun, 1995). F is an important substitutive element for hydroxyl groups and can always form complex solid solution series. Topaz, a typical mineral in the  $\text{Al}_2\text{O}_3$ - $\text{SiO}_2$ - $\text{H}_2\text{O}$  ternary system along with F (ASH + F), could be a potential carrier of  $\text{H}_2\text{O}$  and F in subduction zones. Although topaz is an accessory mineral in the subduction zones and the possible volume of topaz in subducting slabs might be limited, consequently the F content carried by topaz should also be limited, but the results regarding the effect of F will provide more comprehensive constraints for the cycling of volatiles. HPHT experiments have demonstrated that OH-endmember topaz could transform to another high-pressure hydrous aluminosilicate mineral-phase egg  $\text{AlSiO}_3\text{OH}$  or decompose into kyanite  $\text{Al}_2\text{SiO}_5$  (or even corundum and stishovite) and  $\text{H}_2\text{O}$  at the base of the upper mantle along the subducting slabs (Ono, 1998). The incor-

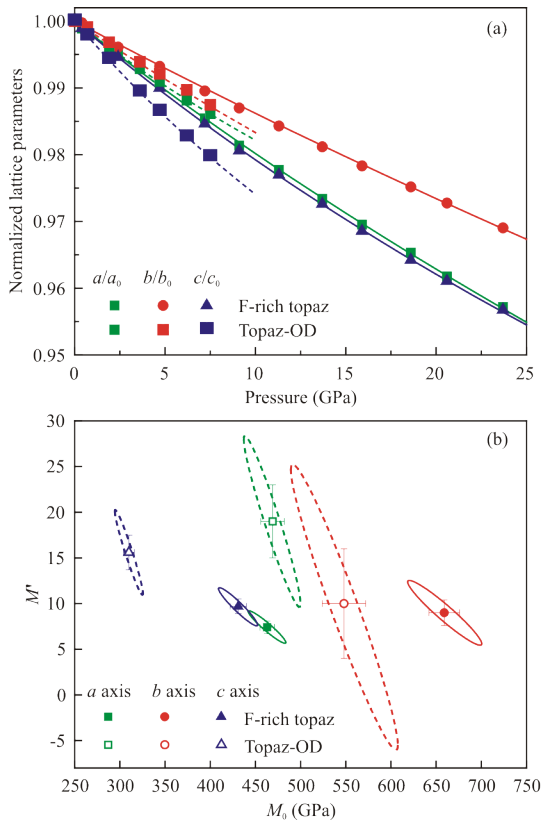


**Figure 5.** (a) Normalized lattice parameters ( $a/a_0$ ,  $b/b_0$ , and  $c/c_0$ ) of topaz as a function of pressure at room temperature. (b) The confidence ellipsoids at the 95.4% level for the  $a$ ,  $b$ , and  $c$  axes, illustrating the trade-off between the linear modulus  $M_0$  and their pressure derivatives  $M$ . Filled and open symbols represent the data for  $\text{Al}_2\text{SiO}_4\text{F}_{1.64}(\text{OH})_{0.36}$  (this study) and  $\text{Al}_2\text{SiO}_4(\text{OH})_2$  (Komatsu et al., 2008), respectively.

poration of F might expand its stability fields to higher temperatures (Liu et al., 2019). Thus, we proposed the following two scenarios, which would be helpful to explain the fate of F and hydroxyl groups in topaz. In the first scenario, F incorporates into the successive hydrous mineral-phase egg, and then it could be transported into the mantle transition zone or even lower mantle (Pamato et al., 2015), which might contribute to enriching the F concentration in the ocean island basalts (Joachim et al., 2015). In the second scenario, F is released from the decomposition of topaz, causing an accumulation of F at the base of the upper mantle. This accumulation could depress the liquidus of mantle minerals and trigger a small degree of partial melting (Beyer et al., 2016), the fractionation of F between melts and minerals would occur, and the incorporated F could influence their properties. Previous experimental studies on halogen partitioning data for partial melting processes at Earth's upper mantle conditions suggested that F is more compatible for silicate minerals (Joachim et al., 2015). It has been confirmed that F has significant effects on the stability of wadsleyite and consequently the depths of the mantle transition zone (Grützner et al., 2018). Accordingly, the properties of hydrous minerals in the ASH system under HPHT conditions would provide important constraints on subduction zones. Here, we have plotted the bulk modulus as a function of density of the minerals in the ASH system based on the experimen-

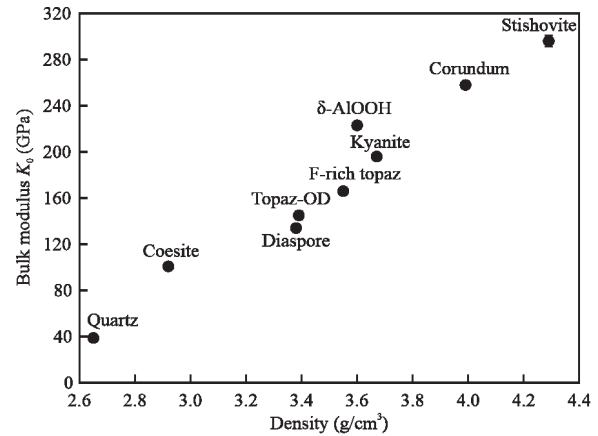


**Figure 6.** The bulk modulus as a function of density of the minerals in the ASH system. The data from literatures are as follows: quartz (Zajonz et al., 1999); coesite (Angel et al., 2001); diaspore (Grevel et al., 2000a); topaz-OD (Komatsu et al., 2008); kyanite (He et al., 2016);  $\delta$ -AlOOH (Duan et al., 2018); corundum (Dubrovinsky et al., 1998); stishovite (Nishihara et al., 2005), the data of F-rich topaz is from this study.

tal results (Fig. 6) (Duan et al., 2018; He et al., 2016; Komatsu et al., 2008; Nishihara et al., 2005; Angel et al., 2001; Grevel et al., 2000a; Zajonz et al., 1999; Dubrovinsky et al., 1998). It is obvious that the isothermal bulk modulus  $K_0$  increases with the increase of density.

We have evaluated the density and bulk velocity profiles of F-rich topaz as a function of pressure along the 1 000 and 1 300 K isotherms (Fig. 7) using the thermoelastic parameters at the lower part of the upper mantle conditions. Our modeled results show that topaz is denser than the preliminary reference Earth model (PREM) (Dziewonski and Anderson, 1981) along both the cold and warm subducting slabs, indicating that the presence of topaz can contribute a positive force for subducting despite its proportion being very limited. The velocities of topaz along the cold and warm slab geotherms are faster than those of the PREM (Dziewonski and Anderson, 1981), which can lead to a strong velocity contrast between the overlying mantle and thin sediment-origin layer. These results are useful for identifying the potential presence of topaz and may provide a constraint on the fine velocity structures in subduction zones. We also compared the density and velocity profiles of topaz with kyanite and phase egg in the ASH ternary system along the 1 300 K isotherm (Schulze et al., 2018; He et al., 2016). Here, we assumed that the thermal elastic parameters ( $\partial K_0/\partial T$  and  $\alpha_0$ ) of the phase egg were the same as those of topaz because there are no available parameters. The transformation from topaz to either kyanite or phase egg will lead to increases in density and bulk sound velocity. Furthermore, different proportions of F/OH substitution in topaz and other hydrous aluminosilicate minerals might significantly affect their physical properties, and knowledge of the lattice preferred orientation of a continuous series of F/OH-bearing solid solutions will provide more constraints on geophysical observations.

#### 4 CONCLUSIONS

In summary, we have investigated the compressibility of F-rich topaz under high  $P$ - $T$  conditions. Our results show that F

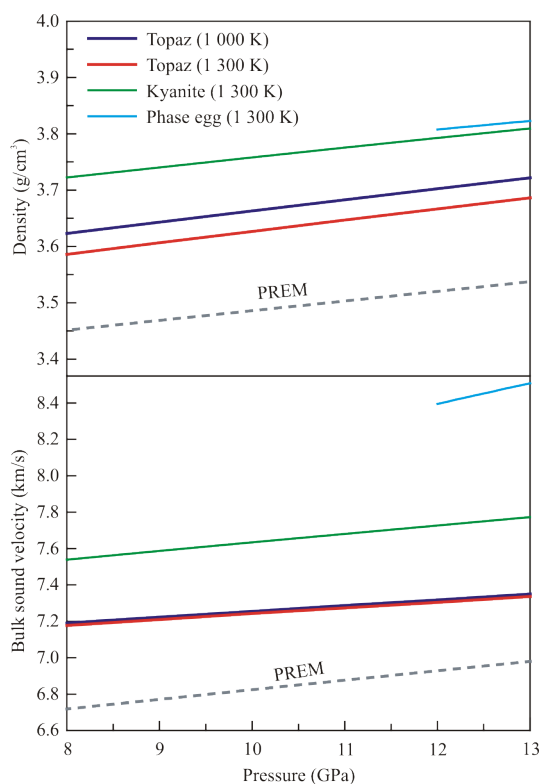


**Figure 7.** Density ( $\rho$ ) and bulk sound velocity ( $V_p$ ) profiles of F-rich topaz compared with kyanite (He et al., 2016) and phase egg (Schulze et al., 2018) along the 1300 K isotherm and the preliminary reference Earth model (PREM) (Dziewonski and Anderson, 1981). Here, we assumed that the temperatures of the cold and warm subduction slabs are 1000 and 1300 K at the depth of the lower part of the upper mantle, respectively.

contents in topaz present significant effects on the isothermal bulk modulus and anisotropic compressibility. And the isothermal bulk modulus  $K_0$  of the minerals in ASH system increases with density. We also propose that large differences in thermal expansivity coefficient of minerals exist extensively, smaller temperature interval and wider temperature range at HPHT conditions will be useful to obtain accurate thermal expansion coefficient. The present modeled results show that the densities and velocities of F-rich topaz are higher than those of the PREM along both the cold and warm subducting slabs. These results are useful for identifying the potential presence of topaz and may provide a constraint on the fine velocity structures in subduction zones.

#### ACKNOWLEDGMENTS

Xiang Wu acknowledges the financial support from the National Science Foundation of China (No. 41827802). We would like to thank Sergey Tkachev for gas loading the diamond anvil cells and Xi Zhu for help in data analysis. This work was performed at GeoSoilEnviroCARS, Advanced Photon Source (APS), Argonne National Laboratory (ANL). GeoSoilEnviroCARS operations were supported by the National Science Foundation-Earth Sciences (No. EAR-1634415) and the Department of Energy, Geosciences (No. DE-FG02-94ER14466). APS was supported by DOE-BES (No. DE-AC02-06CH11357). PX2 and the GSECARS/COMPRES gas loading

system are supported in part by COMPRES under NSF Cooperative Agreement EAR-1661511. The final publication is available at Springer via <https://doi.org/10.1007/s12583-021-1418-y>.

**Electronic Supplementary Materials:** Supplementary materials (Figs. S1–S3; Tables S1–S3) are available in the online version of this article at <https://doi.org/10.1007/s12583-021-1418-y>.

#### REFERENCES CITED

- Angel, R. J., 2000. Equations of State. *Reviews in Mineralogy and Geochemistry*, 41(1): 35–59. <https://doi.org/10.2138/rmg.2000.41.2>
- Angel, R. J., Mosenfelder, J. L., Shaw, C. S. J., 2001. Anomalous Compression and Equation of State of Coesite. *Physics of the Earth and Planetary Interiors*, 124(1/2): 71–79. [https://doi.org/10.1016/s0031-9201\(01\)00184-4](https://doi.org/10.1016/s0031-9201(01)00184-4)
- Angel, R. J., Alvaro, M., Gonzalez-Platas, J., 2014. EosFit7c and a Fortran Module (Library) for Equation of State Calculations. *Zeitschrift Für Kristallographie-Crystalline Materials*, 229(5): 405–419. <https://doi.org/10.1515/zkri-2013-1711>
- Balcone-Boissard, H., Villemant, B., Boudon, G., 2010. Behavior of Halogens during the Degassing of Felsic Magmas. *Geochemistry Geophysics Geosystems*, 11(9): Q09005. <https://doi.org/10.1029/2010gc003028>
- Barnes, J. D., Manning, C. E., Scambelluri, M., et al., 2018. The Behavior of Halogens during Subduction-Zone Processes. Springer Geochemistry. Springer International Publishing, Cham. 545–590. [https://doi.org/10.1007/978-3-319-61667-4\\_8](https://doi.org/10.1007/978-3-319-61667-4_8)
- Beyer, C., Klemme, S., Grützner, T., et al., 2016. Fluorine Partitioning between Eclogitic Garnet, Clinopyroxene, and Melt at Upper Mantle Conditions. *Chemical Geology*, 437: 88–97. <https://doi.org/10.1016/j.chemgeo.2016.05.032>
- Boehler, R., 2006. New Diamond Cell for Single-Crystal X-Ray Diffraction. *Review of Scientific Instruments*, 77(11): 115103. <https://doi.org/10.1063/1.2372734>
- Bucher, K., Stober, I., 2019. Interaction of Mantle Rocks with Crustal Fluids: Sagvandites of the Scandinavian Caledonides. *Journal of Earth Science*, 30(6): 1084–1094. <https://doi.org/10.1007/s12583-019-1257-2>
- Bureau, H., Keppler, H., Métrich, N., 2000. Volcanic Degassing of Bromine and Iodine: Experimental Fluid/Melt Partitioning Data and Applications to Stratospheric Chemistry. *Earth and Planetary Science Letters*, 183(1/2): 51–60. [https://doi.org/10.1016/s0012-821x\(00\)00258-2](https://doi.org/10.1016/s0012-821x(00)00258-2)
- Chen, J., Lager, G. A., 2005. High-Pressure Infrared and Powder X-Ray Study of Topaz-OH: Comparison with Hydrous Magnesium Silicate (Humite). COMPRES 4th Annual Meeting. Jun. 16–19, 2005, New Paltz
- Chen, J. R., Lager, G. A., Kunz, M., et al., 2005. A Rietveld Refinement Using Neutron Powder Diffraction Data of a Fully Deuterated Topaz,  $\text{Al}_2\text{SiO}_4(\text{OD})_2$ . *Acta Crystallographica Section E Structure Reports Online*, 61(11): 253–255. <https://doi.org/10.1107/s1600536805034811>
- Churakov, S. V., Wunder, B., 2004. Ab-Initio Calculations of the Proton Location in Topaz-OH,  $\text{Al}_2\text{SiO}_4(\text{OH})_2$ . *Physics and Chemistry of Minerals*, 31(3): 131–141. <https://doi.org/10.1007/s00269-003-0365-8>
- Duan, Y., Sun, N., Wang, S., et al., 2018. Phase Stability and Thermal Equation of State of  $\delta$ -AlOOH: Implication for Water Transportation to the Deep Lower Mantle. *Earth and Planetary Science Letters*, 494: 92–98. <https://doi.org/10.1016/j.epsl.2018.05.003>
- Dubrovinsky, L. S., Saxena, S. K., Lazor, P., 1998. High-Pressure and High-Temperature *in situ* X-Ray Diffraction Study of Iron and Corundum to

- 68 GPa Using an Internally Heated Diamond Anvil Cell. *Physics and Chemistry of Minerals*, 25(6): 434 – 441. <https://doi.org/10.1007/s002690050133>
- Dziewonski, A. M., Anderson, D. L., 1981. Preliminary Reference Earth Model. *Physics of the Earth and Planetary Interiors*, 25(4): 297–356. [https://doi.org/10.1016/0031-9201\(81\)90046-7](https://doi.org/10.1016/0031-9201(81)90046-7)
- Faccenda, M., 2014. Water in the Slab: A Trilogy. *Tectonophysics*, 614: 1–30. <https://doi.org/10.1016/j.tecto.2013.12.020>
- Fan, D. W., Zhou, W. G., Wei, S. Y., et al., 2010. A Simple External Resistance Heating Diamond Anvil Cell and Its Application for Synchrotron Radiation X-Ray Diffraction. *Review of Scientific Instruments*, 81(5): 053903. <https://doi.org/10.1063/1.3430069>
- Fei, Y. W., 1995. Thermal Expansion. In: Ahrens, T. J., ed., *Mineral Physics and Crystallography, A Handbook of Physical Constants*. Am Geophys Union, Washington, DC
- Fei, Y. W., Ricolleau, A., Frank, M., et al., 2007. Toward an Internally Consistent Pressure Scale. *Proceedings of the National Academy of Sciences of the United States of America*, 104(22): 9182–9186. <https://doi.org/10.1073/pnas.0609013104>
- Friedrich, A., Lager, G. A., Ulmer, P., et al., 2002. High-Pressure Single-Crystal X-Ray and Powder Neutron Study of F, OH/OD-Chondrodite: Compressibility, Structure, and Hydrogen Bonding. *American Mineralogist*, 87(7): 931–939. <https://doi.org/10.2138/am-2002-0716>
- Galvez, M. E., Connolly, J. A. D., Manning, C. E., 2016. Implications for Metal and Volatile Cycles from the pH of Subduction Zone Fluids. *Nature*, 539(7629): 420–424. <https://doi.org/10.1038/nature20103>
- Gatta, G. D., Nestola, F., Ballaran, T. B., 2006. Elastic Behaviour and Structural Evolution of Topaz at High Pressure. *Physics and Chemistry of Minerals*, 33(4): 235 – 242. <https://doi.org/10.1007/s00269-006-0075-0>
- Gatta, G. D., Morgenroth, W., Dera, P., et al., 2014. Elastic Behavior and Pressure-Induced Structure Evolution of Topaz up to 45 GPa. *Physics and Chemistry of Minerals*, 41(8): 569–577. <https://doi.org/10.1007/s00269-014-0670-4>
- Gonzalez-Platas, J., Alvaro, M., Nestola, F., et al., 2016. EosFit7-GUI: A New Graphical User Interface for Equation of State Calculations, Analyses and Teaching. *Journal of Applied Crystallography*, 49(4): 1377–1382. <https://doi.org/10.1107/s1600576716008050>
- Grevel, K. D., Burchard, M., Faßhauer, D. W., et al., 2000a. Pressure-Volume-Temperature Behavior of Diaspore and Corundum: An *in situ* X-Ray Diffraction Study Comparing Different Pressure Media. *Journal of Geophysical Research: Solid Earth*, 105(B12): 27877 – 27887. <https://doi.org/10.1029/2000jb900323>
- Grevel, K. D., Fasshauer, D. W., Rohling, S., 2000b. Bulk Moduli and *P-V-T* Data of the High-Pressure Phases Topaz-OH,  $\text{Al}_2\text{SiO}_4(\text{OH})_2$ , and Phase Pi,  $\text{Al}_3\text{Si}_2\text{O}_7(\text{OH})_3$ . In: EMPG VIII, Eighth International Symposium on Experimental Mineralogy, Petrology and Geochemistry. *Journal of Conference Abstracts*, 5: 1
- Grützner, T., Klemme, S., Rohrbach, A., et al., 2018. The Effect of Fluorine on the Stability of Wadsleyite: Implications for the Nature and Depths of the Transition Zone in the Earth's Mantle. *Earth and Planetary Science Letters*, 482: 236–244. <https://doi.org/10.1016/j.epsl.2017.11.011>
- Hartwig, J., Galkin, V., 2021. Heat Capacity, Thermal Expansion, and Elastic Parameters of Pyrope. *Journal of Thermal Analysis and Calorimetry*, 144(1): 71–79. <https://doi.org/10.1007/s10973-020-09396-2>
- He, Q., Liu, X., Li, B. S., et al., 2016. Thermal Equation of State of a Natural Kyanite up to 8.55 GPa and 1 273 K. *Matter and Radiation at Extremes*, 1(5): 269–276. <https://doi.org/10.1016/j.mre.2016.07.003>
- Holland, T. J. B., Redfern, S. A. T., 1997. Unit Cell Refinement from Powder Diffraction Data: The Use of Regression Diagnostics. *Mineralogical Magazine*, 61(404): 65 – 77. <https://doi.org/10.1180/minmag.1997.061.404.07>
- Huang, S. X., Qin, S., Wu, X., 2019. Elasticity and Anisotropy of the Pyrite-Type  $\text{FeO}_2\text{H-FeO}_2$  System in Earth's Lowermost Mantle. *Journal of Earth Science*, 30(6): 1293–1301. <https://doi.org/10.1007/s12583-018-0836-y>
- Hughes, L., Pawley, A., 2019. Fluorine Partitioning between Humite-Group Minerals and Aqueous Fluids: Implications for Volatile Storage in the Upper Mantle. *Contributions to Mineralogy and Petrology*, 174(9): 78. <https://doi.org/10.1007/s00410-019-1614-2>
- Joachim, B., Pawley, A., Lyon, I. C., et al., 2015. Experimental Partitioning of F and Cl between Olivine, Orthopyroxene and Silicate Melt at Earth's Mantle Conditions. *Chemical Geology*, 416: 65–78. <https://doi.org/10.1016/j.chemgeo.2015.08.012>
- Kantor, I., Prakapenka, V., Kantor, A., et al., 2012. BX90: A New Diamond Anvil Cell Design for X-Ray Diffraction and Optical Measurements. *Review of Scientific Instruments*, 83(12): 125102. <https://doi.org/10.1063/1.4768541>
- Komatsu, K., Kuribayashi, T., Kudoh, Y., 2003. Effect of Temperature and Pressure on the Crystal Structure of Topaz,  $\text{Al}_2\text{SiO}_4(\text{OH},\text{F})_2$ . *Journal of Mineralogical and Petrological Sciences*, 98(5): 167–180. <https://doi.org/10.2465/jmps.98.167>
- Komatsu, K., Kagi, H., Marshall, W. G., et al., 2008. Pressure Dependence of the Hydrogen-Bond Geometry in Topaz-OD from Neutron Powder Diffraction. *American Mineralogist*, 93(1): 217 – 227. <https://doi.org/10.2138/am.2008.2483>
- Kroll, H., Kirfel, A., Heinemann, R., et al., 2012. Volume Thermal Expansion and Related Thermophysical Parameters in the Mg, Fe Olivine Solid-Solution Series. *European Journal of Mineralogy*, 24(6): 935–956. <https://doi.org/10.1127/0935-1221/2012/0024-2235>
- Li, X., Liu, Y. G., Song, H. P., et al., 2020. Thermal Stability and Compressibility of Bastnaesite. *Physics and Chemistry of Minerals*, 47(3): 1–10. <https://doi.org/10.1007/s00269-020-01084-9>
- Li, X. Y., Zhang, C., Wang, L. X., et al., 2020. Experiments on the Saturation of Fluorite in Magmatic Systems: Implications for Maximum F Concentration and Fluorine-Cation Bonding in Silicate Melt. *Journal of Earth Science*, 31(3): 456 – 467. <https://doi.org/10.1007/s12583-020-1305-y>
- Liu, D., Pang, Y. W., Ye, Y., et al., 2019. *In-situ* High-Temperature Vibrational Spectra for Synthetic and Natural Clinohumite: Implications for Dense Hydrous Magnesium Silicates in Subduction Zones. *American Mineralogist*, 104(1): 53–63. <https://doi.org/10.2138/am-2019-6604>
- McDonough, W. F., Sun, S. S., 1995. The Composition of the Earth. *Chemical Geology*, 120(3/4): 223–253. [https://doi.org/10.1016/0009-2541\(94\)00140-4](https://doi.org/10.1016/0009-2541(94)00140-4)
- Momma, K., Izumi, F., 2011. VESTA 3 for Three-Dimensional Visualization of Crystal, Volumetric and Morphology Data. *Journal of Applied Crystallography*, 44(6): 1272 – 1276. <https://doi.org/10.1107/s0021889811038970>
- Mookherjee, M., Tsuchiya, J., Hariharan, A., 2016. Crystal Structure, Equation of State, and Elasticity of Hydrous Aluminosilicate Phase, Topaz-OH ( $\text{Al}_2\text{SiO}_4(\text{OH})_2$ ) at High Pressures. *Physics of the Earth and Planetary Interiors*, 251: 24–35. <https://doi.org/10.1016/j.pepi.2015.11.006>
- Nakagawa, T., 2017. On the Numerical Modeling of the Deep Mantle Water Cycle in Global-Scale Mantle Dynamics: The Effects of the Water



- Solubility Limit of Lower Mantle Minerals. *Journal of Earth Science*, 28(4): 563–577. <https://doi.org/10.1007/s12583-017-0755-3>
- Nishi, M., Irifune, T., Tsuchiya, J., et al., 2014. Stability of Hydrous Silicate at High Pressures and Water Transport to the Deep Lower Mantle. *Nature Geoscience*, 7(3): 224–227. <https://doi.org/10.1038/ngeo2074>
- Nishihara, Y., Takahashi, E., Matsukage, K., et al., 2003. Thermal Equation of State of Omphacite. *American Mineralogist*, 88(1): 80–86. <https://doi.org/10.2138/am-2003-0110>
- Nishihara, Y., Nakayama, K., Takahashi, E., et al., 2005. *P-V-T* Equation of State of Stishovite to the Mantle Transition Zone Conditions. *Physics and Chemistry of Minerals*, 31(10): 660–670. <https://doi.org/10.1007/s00269-004-0426-7>
- Northrup, P. A., Leinenweber, K., Parise, J. B., 1994. The Location of H in the High-Pressure Synthetic  $\text{Al}_2\text{SiO}_4(\text{OH})_2$  Topaz Analogue. *American Mineralogist*, 79(3/4): 401–404
- Ohtani, E., Yuan, L., Ohira, I., et al., 2018. Fate of Water Transported into the Deep Mantle by Slab Subduction. *Journal of Asian Earth Sciences*, 167: 2–10. <https://doi.org/10.1016/j.jseas.2018.04.024>
- Ono, S., 1998. Stability Limits of Hydrous Minerals in Sediment and Mid-Ocean Ridge Basalt Compositions: Implications for Water Transport in Subduction Zones. *Journal of Geophysical Research: Solid Earth*, 103(B8): 18253–18267. <https://doi.org/10.1029/98jb01351>
- Pagé, L., Hattori, K., de Hoog, J. C. M., et al., 2016. Halogen (F, Cl, Br, I) Behaviour in Subducting Slabs: A Study of Lawsonite Blueschists in Western Turkey. *Earth and Planetary Science Letters*, 442: 133–142. <https://doi.org/10.1016/j.epsl.2016.02.054>
- Pagé, L., Hattori, K., Guillot, S., 2018. Mantle Wedge Serpentinites: A Transient Reservoir of Halogens, Boron, and Nitrogen for the Deeper Mantle. *Geology*, 46(10): 883–886. <https://doi.org/10.1130/g45204.1>
- Pamato, M. G., Myhill, R., Ballaran, B. T., et al., 2015. Lower-Mantle Water Reservoir Implied by the Extreme Stability of a Hydrous Aluminosilicate. *Nature Geoscience*, 8(1): 75–79. <https://doi.org/10.1038/ngeo2306>
- Pinheiro, M. V. B., Fantini, C., Krambrock, K., et al., 2002. OH/F Substitution in Topaz Studied by Raman Spectroscopy. *Physical Review B*, 65(10): 104301. <https://doi.org/10.1103/physrevb.65.104301>
- Prescher, C., Prakapenka, V. B., 2015. DIOPTAS: A Program for Reduction of Two-Dimensional X-Ray Diffraction Data and Data Exploration. *High Pressure Research*, 35(3): 223–230. <https://doi.org/10.1080/08957959.2015.1059835>
- Qin, F., Wu, X., Zhang, D. Z., et al., 2017. Thermal Equation of State of Natural Ti-Bearing Clinohumite. *Journal of Geophysical Research: Solid Earth*, 122(11): 8943–8951. <https://doi.org/10.1002/2017jb014827>
- Rivers, M., Prakapenka, V. B., Kubo, A., et al., 2008. The COMPRES/GSECARS Gas-Loading System for Diamond Anvil Cells at the Advanced Photon Source. *High Pressure Research*, 28(3): 273–292. <https://doi.org/10.1080/08957950802333593>
- Ross, N. L., Crichton, W. A., 2001. Compression of Synthetic Hydroxylclinohumite [ $\text{Mg}_9\text{Si}_4\text{O}_{16}(\text{OH})_2$ ] and Hydroxylchondrodite [ $\text{Mg}_5\text{Si}_2\text{O}_8(\text{OH})_2$ ]. *American Mineralogist*, 86(9): 990–996. <https://doi.org/10.2138/am-2001-8-905>
- Sano-Furukawa, A., Kagi, H., Nagai, T., et al., 2009. Change in Compressibility of -AlOOH and -AlOOD at High Pressure: A Study of Isotope Effect and Hydrogen-Bond Symmetrization. *American Mineralogist*, 94(8/9): 1255–1261. <https://doi.org/10.2138/am.2009.3109>
- Schulze, K., Pamato, M. G., Kurnosov, A., et al., 2018. High-Pressure Single-Crystal Structural Analysis of  $\text{AlSiO}_3\text{OH}$  Phase Egg. *American Mineralogist*, 103(12): 1975–1980. <https://doi.org/10.2138/am-2018-6562>
- Straub, S. M., Layne, G. D., 2003. The Systematics of Chlorine, Fluorine, and Water in Izu Arc Front Volcanic Rocks: Implications for Volatile Recycling in Subduction Zones. *Geochimica et Cosmochimica Acta*, 67(21): 4179–4203. [https://doi.org/10.1016/s0016-7037\(03\)00307-7](https://doi.org/10.1016/s0016-7037(03)00307-7)
- Tennakoon, S., Peng, Y., Mookherjee, M., et al., 2018. Single Crystal Elasticity of Natural Topaz at High-Temperatures. *Scientific Reports*, 8: 1372. <https://doi.org/10.1038/s41598-017-17856-3>
- Turner, S., Caulfield, J., Turner, M., et al., 2012. Recent Contribution of Sediments and Fluids to the Mantle's Volatile Budget. *Nature Geoscience*, 5(1): 50–54. <https://doi.org/10.1038/ngeo1325>
- Ulian, G., Valdrè, G., 2017. Effects of Fluorine Content on the Elastic Behavior of Topaz [ $\text{Al}_2\text{SiO}_4(\text{F},\text{OH})_2$ ]. *American Mineralogist*, 102(2): 347–356. <https://doi.org/10.2138/am-2017-5668>
- Wang, X., Xu, X. X., Ye, Y., et al., 2019. *In-situ* High-Temperature XRD and FTIR for Calcite, Dolomite and Magnesite: Anharmonic Contribution to the Thermodynamic Properties. *Journal of Earth Science*, 30(5): 964–976. <https://doi.org/10.1007/s12583-019-1236-7>
- Wang, Z. H., Shi, F., Zhang, J. F., 2020. Effects of Water on the Rheology of Dominant Minerals and Rocks in the Continental Lower Crust: A Review. *Journal of Earth Science*, 31(6): 1170–1182. <https://doi.org/10.1007/s12583-020-1307-9>
- Watenphul, A., Libowitzky, E., Wunder, B., et al., 2010. The OH Site in Topaz: An IR Spectroscopic Investigation. *Physics and Chemistry of Minerals*, 37(9): 653–664. <https://doi.org/10.1007/s00269-010-0365-4>
- Wunder, B., Rubie, D. C., Ross, C. R. II, et al., 1993. Synthesis, Stability and Properties and of  $\text{Al}_2\text{SiO}_4(\text{OH})_2$ : A Fully Hydrated Analogue of Topaz. *American Mineralogist*, 78(3/4): 285–297
- Wunder, B., Andrut, M., Wirth, R., 1999. High-Pressure Synthesis and Properties of OH-Rich Topaz. *European Journal of Mineralogy*, 11(5): 803–814. <https://doi.org/10.1127/ejm/11/5/0803>
- Ye, Y., Smyth, J. R., Jacobsen, S. D., et al., 2013. Crystal Chemistry, Thermal Expansion, and Raman Spectra of Hydroxyl-Clinohumite: Implications for Water in Earth's Interior. *Contributions to Mineralogy and Petrology*, 165: 563–574. <https://doi.org/10.1007/s00410-012-0823-8>
- Yoshino, T., Jaseem, V., 2018. Fluorine Solubility in Bridgmanite: A Potential Fluorine Reservoir in the Earth's Mantle. *Earth and Planetary Science Letters*, 504: 106–114. <https://doi.org/10.1016/j.epsl.2018.10.009>
- Zajonz, J. K., Werner, S., Schulz, H., 1999. High Pressure Single Crystal X-Ray Diffraction Study on  $\alpha$ -Quartz. *Zeitschrift für Kristallographie-Crystalline Materials*, 214(6): 324–330. <https://doi.org/10.1524/zkri.1999.214.6.324>
- Zhang, D. Z., Dera, P. K., Eng, P. J., et al., 2017. High Pressure Single Crystal Diffraction at  $\text{PX}^2$ . *Journal of Visualized Experiments*, (119): 54660. <https://doi.org/10.3791/54660>
- Zhang, R. Y., Liou, J. G., Shu, J. F., 2002. Hydroxyl-Rich Topaz in High-Pressure and Ultrahigh-Pressure Kyanite Quartzites, with Retrograde Woodhouseite, from the Sulu Terrane, Eastern China. *American Mineralogist*, 87(4): 445–453. <https://doi.org/10.2138/am-2002-0408>
- Zhu, G. Z., Gerya, T., Yuen, D. A., 2011. Melt Evolution above a Spontaneously Retreating Subducting Slab in a Three-Dimensional Model. *Journal of Earth Science*, 22(2): 137–142. <https://doi.org/10.1007/s12583-011-0165-x>